



## Uncertainty analysis of earthquake source parameters determined from InSAR: A simulation study

John Dawson<sup>1,2</sup> and Paul Tregoning<sup>1</sup>

Received 6 June 2007; revised 7 June 2007; accepted 20 June 2007; published 27 September 2007.

[1] We assessed the accuracy of earthquake source parameters inverted from simulated Interferometric Synthetic Aperture Radar (InSAR) data. Using focal mechanisms of Australian earthquakes (1959 to the present), we simulated synthetic two-pass InSAR observations with realistic spatial noise derived from the characteristics of actual ERS-2 and ENVISAT InSAR data observed over Australia. The precision of two-pass satellite SAR interferometry with ERS-2 and ENVISAT SAR data in the Australian region can approach  $\pm 2$  mm ( $1\sigma$ ) and is routinely at the  $\pm 4$  mm level. The use of spatially correlated observational weights has minimal impact on the accuracy of earthquake source parameters inverted from InSAR data. In most cases single geometry (i.e., ascending or descending) InSAR observations can be used to accurately determine earthquake source parameters, although typically a combined geometry reduces the source parameter uncertainties by a factor of 1.5. In general, earthquakes of magnitude  $< 4.8$  are unlikely to be observable by InSAR although very shallow events would be detectable. InSAR is insensitive to magnitude 6.2 earthquakes deeper than 10 km, and magnitude 5.5 deeper than 6 km. For earthquake magnitudes  $\geq 5.8$  (average depth 6.5 km) we could estimate the epicenter of the rupture with an average accuracy of 0.25 km, depth to within 0.5 km and the fault orientation to better than  $2^\circ$ . Our findings, based on simulated Australian earthquakes, are representative of typical intraplate earthquakes and would be valid in many other regions. To date no actual earthquakes have been observed by InSAR in Australia.

**Citation:** Dawson, J., and P. Tregoning (2007), Uncertainty analysis of earthquake source parameters determined from InSAR: A simulation study, *J. Geophys. Res.*, 112, B09406, doi:10.1029/2007JB005209.

### 1. Introduction

[2] The estimation of earthquake source parameters from seismic data depends strongly on the data type used, the inversion technique and the complexity of the rupture process [e.g., *Delouis et al.*, 2002; *Salichon et al.*, 2003]. Epicenters and origin times are often poorly separated and, as a result, many estimates have large uncertainties, in particular in depth [*Wright*, 2002]. Interferometric Synthetic Aperture Radar (InSAR) has been widely used for the investigation of earthquakes, in particular to estimate the earthquake source parameters (epicenter, depth, fault dimension, strike, dip, average slip and moment) [*Pedersen et al.*, 2003]. InSAR provides high spatial resolution of surface deformation [e.g., *Massonnet and Feigl*, 1995; *Shamir et al.*, 2003; *Salichon et al.*, 2003] and can provide good constraints on the epicenters and depths of events [*Baumont et al.*, 2004; *Bos et al.*, 2004]. However, the errors associated with InSAR observations are not well understood [*Feigl*, 2002] nor are the errors in InSAR-derived earthquake source parameters.

[3] *Arnadottir et al.* [1992] showed that incorrectly modeled (geodetic) observation correlations can bias earthquake source parameter estimates. The treatment of InSAR observational errors in geophysical modeling applications varies considerably. Some studies have assigned equal weights to all observations in their analysis [e.g., *Amelung and Bell*, 2003; *Schmidt and Burgmann*, 2006] while others have used spatially uncorrelated observational weights (i.e., diagonal covariance matrices) [e.g., *Pritchard and Simons*, 2002; *Simons et al.*, 2002; *Wright et al.*, 2004]. More sophisticated approaches have included the use of realistic spatially correlated noise, assuming that the spatial process is stationary and isotropic [*Wright et al.*, 2004; *Funning et al.*, 2005; *Lohman and Simons*, 2005b].

[4] The assessment of the uncertainties and parameter trade-offs of estimated earthquake source parameters, derived from InSAR observations, can be undertaken by inverting a series of simulated interferograms with realistically correlated noise. Such assessments have been completed for a number of specific earthquakes [*Wright et al.*, 2004; *Funning et al.*, 2005; *Lohman and Simons*, 2005a; *Talebian et al.*, 2006], but not for a broad general set of events. The sensitivity of InSAR to detect and characterize small events has also only received limited attention [*Mellors et al.*, 2004; *Lohman and Simons*, 2005b].

<sup>1</sup>Research School of Earth Sciences, The Australian National University, Canberra, Australia.

<sup>2</sup>Also at Geoscience Australia, Canberra.

[5] In this study we assessed the use of InSAR for earthquake source parameter determination, through the simulation and inversion of a range of representative earthquakes in Australia. Specifically, the aims of this paper were (1) to investigate spatial noise structures in Australian interferograms, (2) to quantify the importance of the treatment of InSAR observational noise in earthquake source parameter inversions, (3) to assess typical elastic dislocation modeling for earthquake source parameter inversions from InSAR data, and (4) to quantify the event types and range of earthquake magnitudes and depths to which InSAR is sensitive and the accuracy of the InSAR-derived models for the earthquakes.

## 2. Synthetic Aperture Radar

### 2.1. Background

[6] Synthetic Aperture Radar (SAR) is a space geodetic technique that has been widely used for the construction of digital elevation models and the detection of small deformations of the Earth's surface. Extensive literature exists [see the reviews by *Massonnet and Feigl*, 1998; *Zebker*, 2000] and will not be explained in detail here. The typical spatial resolution of a satellite SAR image is approximately  $20 \times 20$  m, with an image swath of around 100 km. Geophysical applications to measure surface deformation using SAR began in the early 1990s and considerable research has focused on surface deformation due to natural processes such as earthquakes [e.g., *Simons et al.*, 2002; *Massonnet et al.*, 1996].

[7] The formation of interferometric and amplitude-matched SAR images from the combination of two or more images (before and after an earthquake) results in the observation of relative surface deformation within the images. Previous studies indicate that, while the accuracy of the technique depends on the specifics of individual image pairs, in low vegetation conditions and with good temporal coverage InSAR can produce interferometric observations (i.e., target to satellite line-of-sight) with a precision of  $\pm 1$  cm and radar amplitude observations (i.e., in the radar azimuth direction) with a precision of  $\pm 10$ – $50$  cm [e.g., *Michel et al.*, 1999; *Fialko et al.*, 2001; *Funning et al.*, 2005]. In this present study we focus on Interferometric SAR (InSAR) observations.

### 2.2. Quantifying Typical InSAR Noise for the Australian Region

[8] InSAR observations contain phase noise caused by, for example radar system noise, atmospheric propagation effects, temporal decorrelation (i.e., resulting from the Earth's surface radar scattering properties changing with time), spatial decorrelation (i.e., resulting from non-zero perpendicular distance between orbit trajectories), platform position error and processing error (e.g., misregistration noise) [*Zebker and Villasenor*, 1992; *Gatelli et al.*, 1994; *Burgmann et al.*, 2000]. Temporal decorrelation can be minimized through the selection of images with small temporal separation while spatial decorrelation can be minimized through the selection of images with small baseline differences (i.e., the distance between the satellite locations at the time the two images were taken). Differences in the Doppler-centroid frequency between acquis-

itions also contributes to observation noise [*Just and Bamler*, 1994]. Incorrect phase unwrapping can also be a significant source of error [*Ghiglia and Pritt*, 1998].

[9] Early investigations of InSAR observational error included the analysis of the spatial spectrum of InSAR data observed in Southern California [*Goldstein*, 1995] and Hawaii [*Zebker et al.*, 1997]. These studies revealed that a significant portion of the observed error could be explained by atmospheric turbulence. *Williams et al.* [1998] applied a covariance model, in space and time, using results originally obtained from Very Long Base Interferometry (VLBI) to InSAR. Later, *Hanssen* [2001] used data observed in the Netherlands to develop one-dimensional (1D) covariance functions for InSAR data by radially averaging a two-dimensional (2D) autocorrelation function obtained using the data power spectrum. These studies clearly demonstrate the spatially correlated nature of noise in InSAR analyzes.

[10] From spectral analyzes and geostatistical techniques, we characterized the typical spatial variability of InSAR data from the ERS-2 and ENVISAT satellites from 1995 to the present (see Table 1). We then generated synthetic noise models that were consistent with typical spatial correlations observed in actual InSAR data, such as noise resulting from the propagation delay of radar observations through the neutral atmosphere [e.g., *Williams et al.*, 1998].

[11] We analyzed pairs of SAR images using the EV-InSAR ATLANTIS software [*Atlantis-Scientific*, 2004]. A 3 arc second digital elevation model from the Shuttle Radar Topography Mission (SRTM) was used to correct for topographic phase and a bilinear phase ramp was removed from each interferogram to account for orbital errors. There is no explicit evidence of surface deformation in any of the analyzed interferograms and no seismic events were recorded in the study area during the period covered by the SAR images. Therefore we assumed that the interferograms consisted of observational noise alone.

[12] Interferograms #2, #7 and #11 have low coherence (Table 1) and we excluded them from further analysis. Good interferograms are formed when the satellite baseline ( $B_{\perp}$ ) is less than 580 m and the temporal separation ( $\Delta t$ ) is less than 175 days. We suggest that these values represent appropriate limits for the generation of interferograms in Australian conditions. The standard deviations of the line-of-sight observations ( $\sigma_{obs}$ ) in the assessed interferograms range from 2.7 to 8.5 mm, with a mean value of 4.7 mm.

[13] In Figure 1 we show a poor and a good quality interferogram (#14 and # 8). The circular features in the center of Figure 1a are associated with atmospheric water vapor present in one SAR image that are not present in other spatially and temporally overlapping interferograms (not shown). These features result in interferogram-equivalent variations of  $\sim 45$  mm line-of-sight range changes and are approximately 5 km in diameter. We used the noise characteristics of this image to represent a worst case scenario. The low coherence 'paddock-shaped' areas in Figure 1b are associated with agricultural activity in the Burakin area.

[14] We computed two-dimensional Fourier transforms of each unwrapped line-of-sight interferogram and the resultant power spectrum in the radial direction (Figure 2). While the absolute power of the noise power spectrum varies, the power law structure is consistent in all interferograms. On spatial scales of 0.5 to 2 km, the spectral slopes are

**Table 1.** InSAR Pairs Used in Spatial Variability Assessment<sup>a</sup>

#	Master Image Acquisition Date	Slave Image Acquisition Date	Satellite	$ B_{\perp} $ , m	$ \Delta t $ , days	$ B_{Dopp} $ , Hz	Lat., deg	Long., deg	Locality	$\sigma_{obs}$ , mm	Comment Date
1.	2004-12-28	2004-11-23	ENVISAT	580.4	35	3	-30.5	117.0	Burakin	6.5	
2.	2005-02-01	2004-12-28	ENVISAT	775.6	35	5	-30.5	117.0	Burakin	12.6	Low coh.
3.	2005-03-08	2004-12-28	ENVISAT	208.4	70	7	-30.5	117.0	Burakin	4.5	
4.	2005-03-08	2005-02-01	ENVISAT	566.9	35	12	-30.4	117.0	Burakin	4.2	
5.	2005-05-17	2005-04-12	ENVISAT	265.6	35	0	-30.4	117.0	Burakin	5.6	
6.	2005-06-21	2005-05-17	ENVISAT	86.0	35	7	-30.4	117.0	Burakin	3.6	
7.	2005-07-26	2005-02-01	ENVISAT	152.5	175	7	-30.5	117.0	Burakin	20.1	Low coh.
8.	2005-07-26	2005-06-21	ENVISAT	321.4	35	4	-30.4	117.0	Burakin	2.7	
9.	2005-10-04	2005-07-26	ENVISAT	136.8	70	43	-30.5	117.0	Burakin	3.6	
10.	2005-10-04	2005-06-21	ENVISAT	184.9	105	39	-30.5	117.0	Burakin	4.2	
11.	2005-10-04	2005-05-17	ENVISAT	99.1	140	32	-30.5	117.0	Burakin	16.6	Low coh.
12.	2005-10-12	2005-09-07	ENVISAT	225.0	35	49	-30.5	116.8	Burakin	3.6	Ascending
13.	1997-03-25	1997-01-14	ERS-2	110.8	70	42	-30.5	116.9	Burakin	3.2	
14.	1995-12-31	1995-11-26	ERS-2	451.4	35	171	-19.9	134.3	Tennant Ck.	8.5	
15.	1996-05-19	1995-11-26	ERS-2	485.6	175	126	-19.9	134.3	Tennant Ck.	4.6	
16.	1996-05-19	1995-12-31	ERS-2	34.2	140	45	-19.9	134.3	Tennant Ck.	7.1	

<sup>a</sup> $B_{\perp}$  is the perpendicular baseline distance between the ‘master’ and ‘slave’ satellite trajectories (computed at the image center point).  $\Delta t$  is the time between the acquisition of the master and slave images.  $B_{Dopp}$  is the difference between the Doppler-centroid frequency of the master and slave images.  $\sigma_{obs}$  is the standard deviation (mm) of the LOS observations over the scene. All ENVISAT acquisitions are in IS2 mode (i.e., target to satellite incidence angle is 23°). All passes are descending with the exception of the ascending ENVISAT 2005-10-12 and 2005-09-07 images. The interferogram area is 60 × 60 km extracted from the center of each processed scene. The interferograms were multilooked by a factor of 5 in azimuth, i.e., a ~20 meter pixel size.

approximately  $-5/3$ , consistent with atmospheric turbulence and previous InSAR investigations [Hanssen, 2001; Jonsson, 2002]. On spatial scales smaller than  $\sim 0.5$  km the spectrum is dominated by noise associated with the radar instrument and radar analysis [Goldstein, 1995; Jonsson, 2002].

[15] Assuming that the noise is spatially stationary and isotropic, we evaluated the covariance functions of the unwrapped line-of-sight interferograms using the structure function [e.g., Agnew, 1992; Williams *et al.*, 1998; Lohman and Simons, 2005a]:

$$S(r) = E[(f(\mathbf{x}) - f(\mathbf{x} + \mathbf{r}))^2] \quad (1)$$

where  $E[\cdot]$  is the ensemble average,  $r$  is the scalar distance between two observations (i.e.,  $r = |\mathbf{r}|$ ) and  $f(\mathbf{x})$  is the observation at some position  $\mathbf{x}$ . The covariance function,  $C_n(r)$ , was then related to the structure function by [Cressie, 1993]:

$$C_n(r) = \sigma^2 - S(r)/2 \quad (2)$$

where  $\sigma^2$  is the variance of noise. In this study these covariance functions are subsequently used to weight the InSAR observations.

[16] We evaluated covariance functions (Figure 3) in the spatial domain using large data samples [Lohman and Simons, 2005a], fitting nested variogram models to the sample variograms by non-linear weighted least squares [Cressie, 1993]. The Tennant Creek interferograms #14 and #16 (Table 1) (which include the common scene containing considerable atmospheric delay effects) produce covariance functions with the two largest magnitudes, as expected.

### 3. Earthquake Modeling

#### 3.1. Simulated Earthquakes

[17] While the majority of global earthquakes occur at plate boundaries, intraplate earthquakes contribute  $\sim 5\%$  of

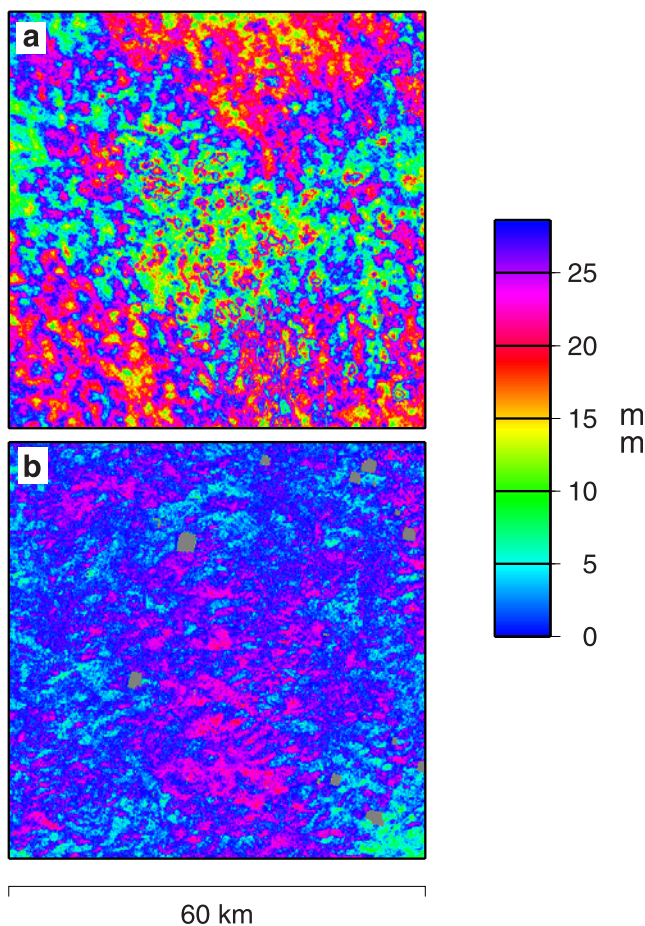


**Figure 1.** Example interferograms (line-of-sight), (a) Interferogram #14, Tennant Creek (ERS-2) November 1995–December 1995. This is taken as a worst case scenario for the noise modeling. (b) Interferogram #8, Burakin (ENVISAT) June 2005–July 2005. This is a typical case of interferogram noise. Grey areas indicate low coherence.

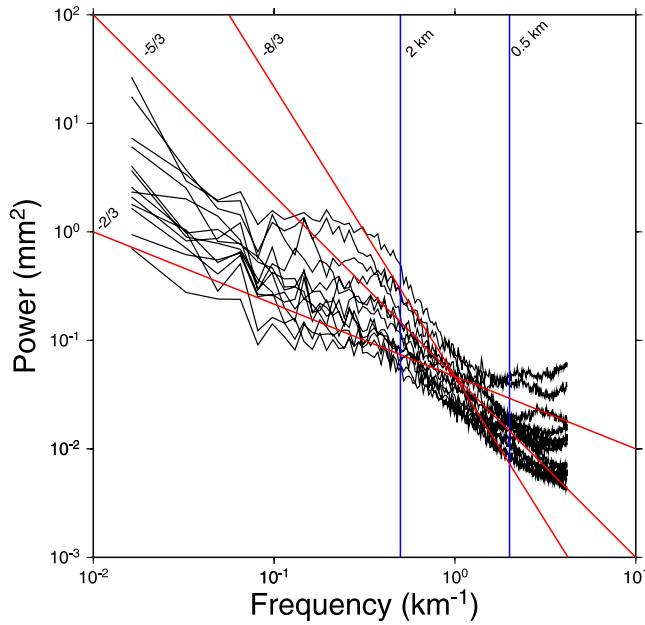


**Figure 2.** Radially averaged power spectra of Australian InSAR interferograms (see Table 1). Diagonal lines represent the  $-8/3$ ,  $-5/3$ ,  $-2/3$  spectral slopes [Agnew, 1992]. Vertical lines represent the 0.5 and 2 km spatial regions. Note that some interferograms have common scenes and are not independent.

global seismic moment release [Scholz, 1990]. Despite Australia being largely regarded as a ‘stable’ plate, large earthquakes occur, with 17 magnitude  $>6$  earthquakes recorded since the installation of seismometers in 1901 [McCue, 1990; Leonard *et al.*, 2002]). Satellite SAR observations of the Australian continent have been made since 1991 from various multiyear, temporally overlapping satellite missions, including ERS-1, ERS-2, JERS-1, RADARSAT and ENVISAT. While highly successful in many international contexts, InSAR has not been utilized to investigate any Australian earthquakes, although its potential to do has been previously noted by Ge *et al.* [2002]. Unfortunately, the ERS SAR data coverage in Australia is limited and has not observed any earthquakes in the period since the launch of the ERS-1 satellite. Therefore we are restricted to only simulations in this study.

[18] We used earthquakes and fault plane solutions detailed by Leonard *et al.* [2002] to simulate surface deformation patterns in the InSAR interferograms. The data set includes 84 earthquakes with magnitudes that range from 2.4 to 6.7, although we discarded earthquakes that did not generate surface deformation detectable by InSAR. Any errors in the actual locations of the events can be ignored, since we wish only to simulate then attempt to recover a deformation signal. We ensured that all modeled earthquakes were not below the average seismogenic layer. Where the subsequent fault plane estimates extended above the surface, the fault depth was adjusted (i.e., increased) so that the rupture was contained within the crust.

[19] Using earthquake moment  $M_w$ , strike, rake, dip and depth and empirical relations, we derived the fault dimensions and slip on which we based our elastic dislocation

modeling. We subsequently estimated the fault width, length and slip. We adopted the regressions of Wells and Coppersmith [1994] as a basis for the computation of the fault dimensions:

$$\log_{10}(W/1000) = -1.01 + 0.32M_w \quad (3)$$

and

$$\log_{10}(L/1000) = -2.44 + 0.59M_w \quad (4)$$

where  $W$  is the fault width (m) and  $L$  is the fault length (m), using the regression coefficients for all event types. Such empirical relationships are not well constrained for small magnitude earthquakes, however the computed fault dimensions remain physically plausible, so for consistency we used them for all magnitude earthquakes.

[20] The seismic moment,  $M_0$ , is then computed using the magnitude relation [Hanks and Kanamori, 1979]:

$$\log_{10}(M_0) = 3/2 (M_w + 10.7). \quad (5)$$

[21] The average slip (m),  $U$ , is computed using the relationship between seismic moment and the fault dimensions [Aki and Richards, 2002]:

$$U = \frac{M_0}{\mu LW} \quad (6)$$

where  $\mu$  is the shear modulus of the Earth’s crust (in this study we adopted  $\mu = 30$  GPa). We assume that the Earth’s crust is well modeled as a Poisson solid. All faults were assumed to be double-couple sources without tensile components and all earthquakes are assumed to have a single rectangular rupture patch with constant slip over the

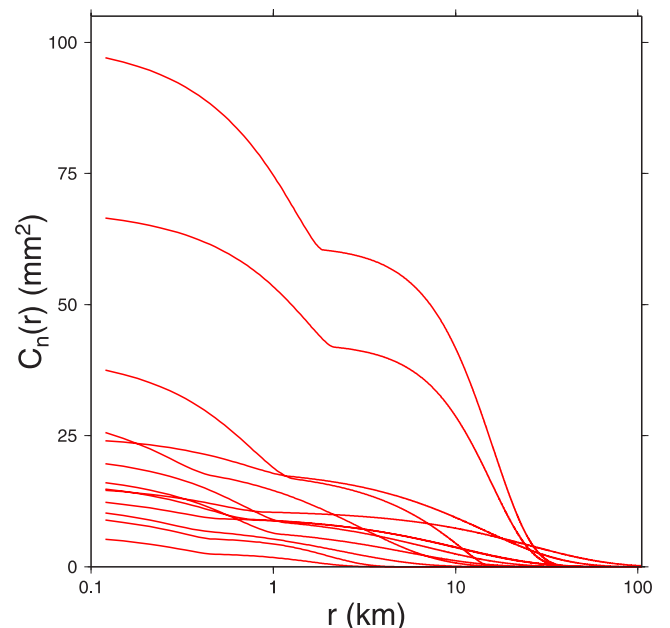


**Figure 3.** Covariance functions  $C_n(r)$  of the assessed interferograms (see Table 1).

**Table 2.** Earthquakes With Significant Modeled Surface Deformation (Sorted Order is Descending Magnitude)<sup>a</sup>

#	$M_w$	Lat., deg	Long., deg	Depth, km	Strike, deg	Dip, deg	Rake, deg	Description	Date dd/mm/yyyy
1.	6.7	-22.05	126.61	15.0	161	45	79	Lake Mackay	24/03/1970
2.	6.6	-31.62	116.98	5.0	351	29	73	Meckering	14/10/1968
3.	6.6	-19.86	133.80	5.0	132	36	107	Tennant Creek C	22/01/1988
4.	6.3	-19.85	133.80	6.0	326	38	114	Tennant Creek A	22/01/1988
5.	6.3	-19.86	133.80	4.8	152	73	154	Tennant Creek B	22/01/1988
6.	6.2	-24.74	136.92	7.0	53	64	31	Simpson Desert	28/08/1972
7.	6.2	-30.83	117.18	3.0	166	26	71	Cadoux	02/06/1979
8. <sup>b</sup>	6.2	-16.05	124.42	10.0	17	84	153	Collier Bay	10/08/1997 <sup>b</sup>
9.	5.9	-31.11	116.47	3.7	157	76	39	Calingiri	10/03/1970
10.	5.8	-26.33	132.52	5.0	350	58	152	Marryat Creek	30/03/1986
11.	5.5	-31.72	116.99	6.0	200	28	120	Meckering	17/01/1990
12. <sup>b</sup>	5.4	-32.92	151.29	1.8	309	44	77	Ellalong	06/08/1994
13. <sup>b</sup>	5.2	-33.61	120.59	1.7	264	48	-90	Ravensthorpe	19/10/2001
14. <sup>b</sup>	5.2	-30.52	117.05	2.0	27	64	90	Burakin	30/03/2002
15.	5.1	-19.79	133.95	3.0	226	34	-131	Tennant Creek	19/06/1991
16. <sup>b</sup>	5.1	-30.08	143.53	2.0	213	64	-136	White Cliffs	13/08/1996
17. <sup>b</sup>	5.1	-30.49	117.06	2.1	103	84	31	Burakin	28/09/2001
18. <sup>b</sup>	5.0	-30.48	117.09	1.3	223	42	-110	Burakin	05/03/2002
19. <sup>b</sup>	4.8	-30.52	117.08	1.6	285	79	-55	Burakin	23/03/2002

<sup>a</sup>Earthquake depth is as adjusted (refer section 3.1). The Tennant Creek earthquakes of the 22/01/1998 are labeled A, B and C and reflect the chronological order of activity on that day. Depth refers to center of rupture patch. ERS-1 launch (17/07/1991).

<sup>b</sup>Post ERS-1 launch (17/07/1991).

entire surface. That this is unrealistic has little impact on the simulation results.

### 3.2. Simulated Deformation

[22] Given the relative data volumes of observed ERS-1/2 and ENVISAT data over Australia, we adopted the general characteristics of these satellites for our simulations. In the synthetic interferograms each fringe (or full color cycle) represents the line-of-sight range change of one half of the radar instrument wavelength,  $\lambda$ , (i.e., ERS-1/2  $\lambda = 56.6$  mm, ENVISAT  $\lambda = 56.2$  mm). In Australia, a typical look direction (target-to-satellite) for an ERS or ENVISAT descending orbit swath is *azimuth* = 103° and *elevation* = 67°, while for an ascending orbit the look direction is *azimuth* = 257° and *elevation* = 67°. line-of-sight displacements (and the corresponding phase observations) were computed using the RNGCHN software [Feigl and Dupre, 1999], based on the elastic dislocation models of Okada [1985]. We simulated the deformation directly in the interferogram rather than in the raw radar data followed by subsequent interferometric analysis.

[23] In the ideal case, phase gradients greater than one fringe per pixel result in total loss of coherence [Massonnet and Feigl, 1998; Hanssen, 2001] but in the presence of observation noise the decorrelation limits are more stringent. We adopted an empirically derived function of maximum phase gradient [Baran *et al.* 2005]:

$$d_{max} = \frac{\lambda}{2\eta} + \frac{\gamma - 1}{500} \quad (7)$$

to provide a limit on the observation availability, using a typical average coherence value ( $\gamma = 0.7$ ) and a pixel size of  $\eta = 20$  m to define our maximum gradient ( $d_{max} = 0.8 \times 10^{-3}$ ). In the cases where the phase gradient exceeds this limit the affected simulated data is masked from further analysis.

### 3.3. Earthquake Detection

[24] The InSAR observation of earthquakes is highly dependent on both the earthquake magnitude and depth. In the case of noise-free interferograms, 19 earthquakes were identified that have modeled displacements detectable from InSAR observations (Table 2 and Figures 4 and 5a). No earthquakes of  $M_w < 4.8$  were detectable (the shallowest undetected small earthquake that we simulated was at 1.3 km depth). Earthquakes of  $4.8 < M_w < 6.2$  were detected, although all occurred at relatively shallow depths ( $\sim 6$  km). All recorded  $M_w > 6.2$  earthquakes were clearly visible down to depths of  $\sim 15$  km. Nine of the 19 detected earthquakes have occurred in the South West Seismic Zone ( $\sim 50\%$ ) in Western Australia. A further 4 earthquakes occurred in the Tennant Creek region with the remaining 6 events occurring in various other localities across the continent.

### 3.4. Simulated Noise and Inversions

[25] To make the earthquake inversion process more realistic we adopted the Burakin (#8) and Tennant Creek (#14) interferograms (from section 2.2) as the basis of low and high noise modeling scenarios. In the low observation noise scenario all the 19 identified earthquakes (with  $M_w > 4.8$ ) are clearly visible (Figure 5b) whereas only earthquakes with  $M_w > 5.8$  are clearly visible in the high observation noise scenario (Figure 5c).

[26] For each earthquake, a series of low and high noise synthetic interferograms was generated, consisting of 100 synthetic noise-only interferograms. The simulated data series were generated by non-conditional simulation [Cressie, 1993] with the variogram modeling being undertaken on the interferograms prior to the addition of the deformation. While the variogram modeling was undertaken on unwrapped data the effects of phase unwrapping error are largely neglected, and considered out of the scope of this paper. We inverted each of the 100 simulated noise-plus-deformation interferograms for each earthquake to estimate the parameters describing the earthquake. The scatter of the

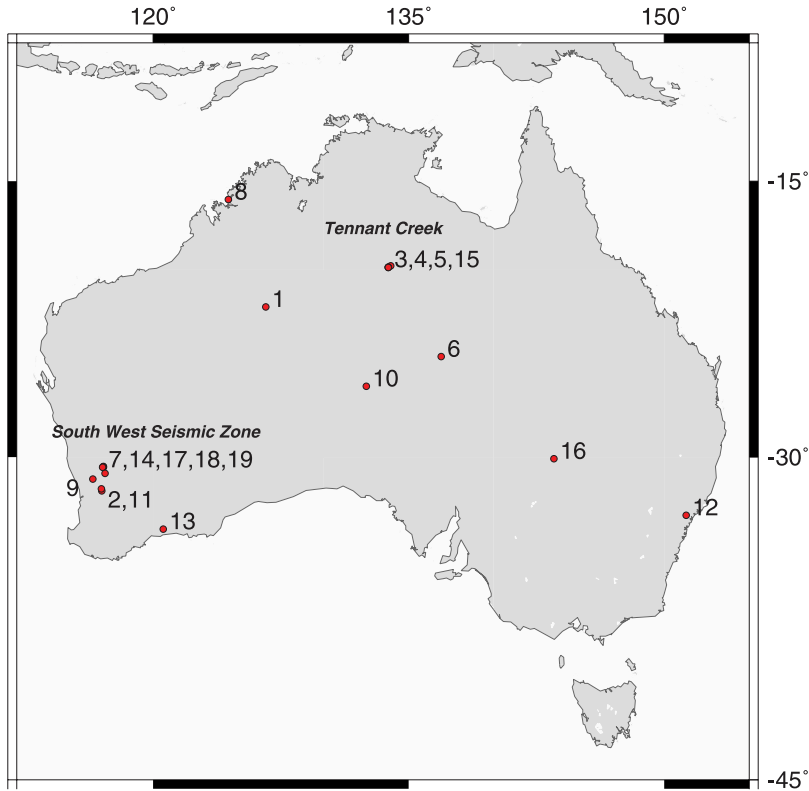


**Figure 4.** Locations of earthquakes with significant visible modeled surface deformation (numbering is from Table 2).

estimates - and any biases away from the true values - provides insight into the actual ability of InSAR analysis to estimate earthquake parameters under good and poor noise conditions.

[27] Unsurprisingly it was not possible to obtain realistic estimates of both the fault patch dimension and slip magnitude for the smaller earthquakes. For earthquakes  $5.4 \leq M_w \leq 5.5$  the rupture fault patch was constrained to be a square rather than estimating the length and width of the fault patch, while for earthquakes  $M_w < 5.4$  the rupture fault patch dimensions were not estimated but constrained to be a fixed size square patch with the dimensions approximated by the average of the value of the rupture length and width used in the simulation.

[28] To reduce the volume of observations to a computationally manageable level the InSAR data were initially down-sampled using a quadtree partitioning algorithm [Jonsson *et al.*, 2002]. The threshold variances used in the quadtree partitioning algorithm were selected so that each earthquake data set contained approximately 1500 observations. As an alternative to averaging the observations within each quadrant, we selected the pixel with the median observation value over the quadrant, and found improved results with this approach. Median sampling also simplifies the covariance computations used in the subsequent inversions. The observation covariances were computed using the covariance functions derived for the data simulations. Our analysis was undertaken assuming the availability of descending and ascending pass data but we also repeated computations assuming only ascending or descending pass

data availability to assess the sensitivity of the parameter estimates to single or dual geometry interferometry.

[29] We performed the inversions using the Direction Set Method [Press *et al.*, 1992] which is iterated with randomly selected prior values for considered parameters (e.g., Wright *et al.* [1999]). The approach yields identical results to the direct search Neighborhood Algorithm [Sambridge, 1999a], but with faster convergence. We used a weighted least squares method where the weight matrix of the observations was computed using the associated 1-dimensional covariance function. The search of parameter space was unconstrained, although the depth, rupture patch length and width parameters were constrained to be positive through the application of auxiliary parameter transforms [e.g., Wright *et al.*, 1999]. We considered the simulated InSAR observations only and made no attempt to constrain the source parameters based on other information, such as seismic or surface rupture observations, as might be the case for actual earthquakes.

#### 4. Results and Discussion

[30] For each simulation series we assessed the accuracies of the estimated parameters by computing the mean parameter bias and the Root Mean Square Error (RMSE):

$$RMSE_i = \sqrt{\frac{1}{n-1} \sum_{j=1}^n (p_i^j - \mu_i)^2} \quad (8)$$

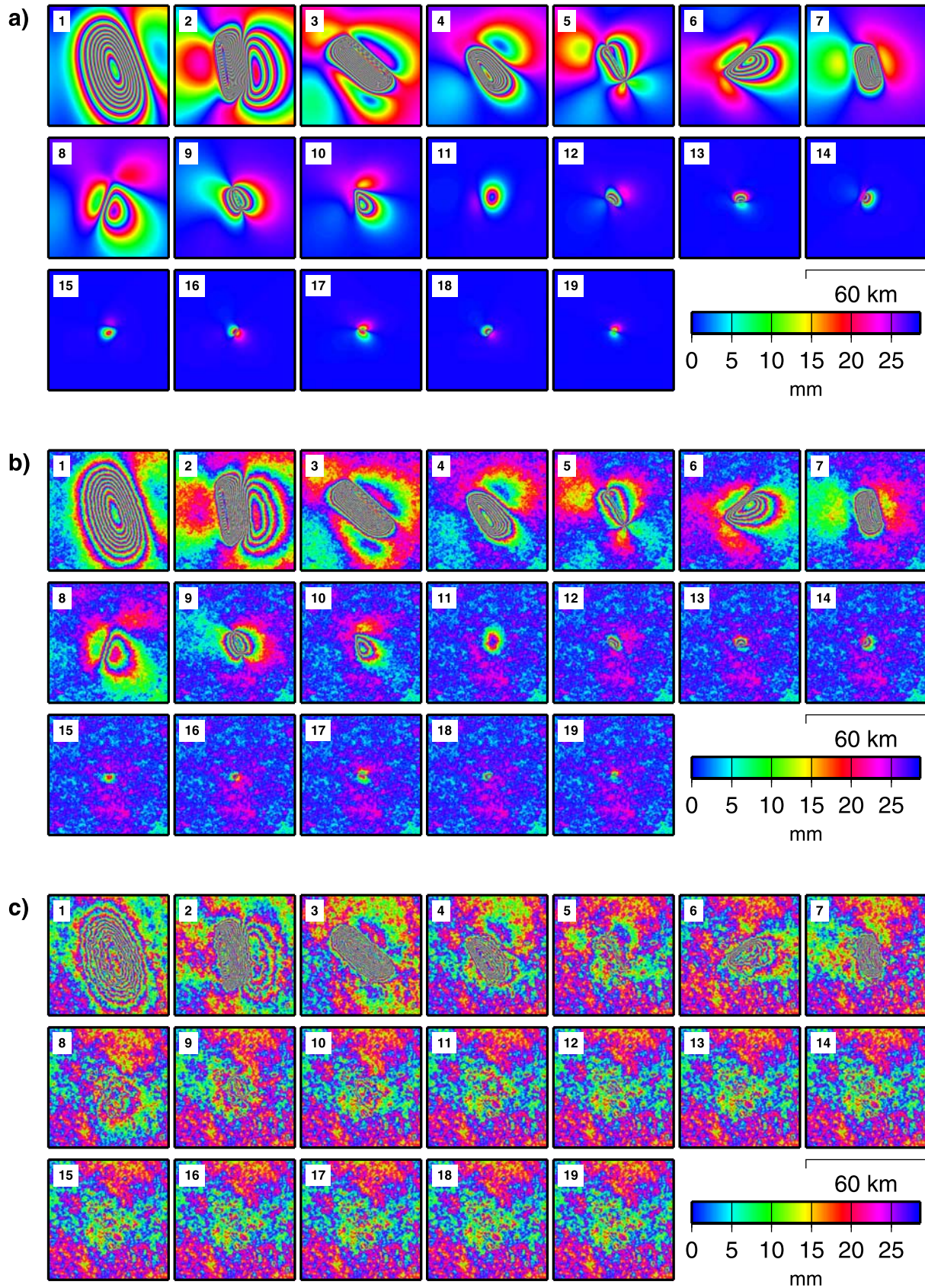


**Figure 5.** Simulated earthquake interferograms. line-of-sight interferometric observations from descending two-pass satellite InSAR (ENVISAT). The center of the earthquake rupture patch is located in the center of each image. The earthquake numbering sequence (1–9) is as per Table 2. (a) No observation noise. (b) Low observation noise. (c) High observation noise.

**Table 3.** Inversion Results<sup>a</sup>

	X, km	Y, km	Depth, deg	Strike, deg	Dip, deg	U1, mm	U2, mm	L, km	W, km	$M_w$	Comment
RMSE <sup>hics</sup>	0.26	0.22	0.51	9.90	4.59	42.2	29.7	0.24	0.51	0.035	Average of all earthquakes
RMSE <sup>hlc</sup>	0.18	0.15	0.39	9.71	3.11	22.2	14.4	0.19	0.42	0.023	excluding Collier Bay (#8)
RMSE <sup>hls</sup>	0.30	0.25	0.57	9.48	5.17	51.4	36.1	0.27	0.57	0.040	Meckering (#11 <sup>b</sup> ).
RMSE <sup>hc</sup>	0.27	0.22	0.59	11.29	4.61	33.5	18.1	0.22	0.59	0.035	
RMSE <sup>lc</sup>	0.09	0.09	0.20	8.22	1.69	11.6	10.9	0.17	0.26	0.011	
RMSE <sup>hics</sup>	0.24	0.16	0.53	0.40	1.77	32.5	16.0	0.18	0.68	0.016	Average of all earthquakes
RMSE <sup>hlc</sup>	0.18	0.11	0.42	0.30	1.29	21.4	12.0	0.14	0.53	0.012	$M_w \geq 5.8$ , excluding #8.
RMSE <sup>hls</sup>	0.27	0.18	0.59	0.44	2.02	38.2	18.1	0.20	0.76	0.019	
RMSE <sup>hc</sup>	0.28	0.16	0.71	0.44	2.01	32.0	17.8	0.21	0.88	0.018	
RMSE <sup>lc</sup>	0.07	0.05	0.14	0.16	0.56	10.7	6.1	0.07	0.19	0.005	
RMSE <sup>hics</sup>	0.29	0.28	0.48	19.77	7.52	52.2	44.0	0.31	0.34	0.055	Average of all earthquakes
RMSE <sup>hlc</sup>	0.18	0.21	0.35	19.67	5.03	23.2	17.0	0.25	0.30	0.035	$M_w \leq 5.5$ , excluding #11 <sup>b</sup> .
RMSE <sup>hls</sup>	0.34	0.32	0.54	19.82	8.76	66.8	57.5	0.34	0.36	0.065	
RMSE <sup>hc</sup>	0.26	0.30	0.46	23.49	7.53	35.2	18.4	0.23	0.26	0.054	
RMSE <sup>lc</sup>	0.11	0.13	0.26	16.28	2.81	12.4	15.7	0.27	0.33	0.018	
RMSE <sup>hc</sup>	0.28	0.22	0.49	4.11	7.44	46.4	9.7	-	-	0.093	Smallest magnitude earthquake.
RMSE <sup>lc</sup>	0.10	0.30	0.40	125.33	7.35	10.9	79.0	-	-	0.028	Burakin $M_w$ 4.8 (#19).
RMSE <sup>hs</sup>	0.63	0.38	0.64	49.42	12.21	121.2	40.7	-	-	0.187	
RMSE <sup>ls</sup>	0.21	0.14	0.44	1.85	4.83	33.5	10.4	-	-	0.070	
RMSE <sup>hc</sup>	0.23	0.19	0.30	1.54	7.35	20.8	7.8	0.33	0.33	0.029	Shallowest earthquake.
RMSE <sup>lc</sup>	0.11	0.07	0.24	0.68	2.04	6.1	3.9	0.33	0.33	0.012	Burakin $M_w$ 5.0 (#18),
RMSE <sup>hs</sup>	0.32	0.24	0.51	2.43	11.29	46.5	13.5	0.33	0.33	0.066	1.3 km depth.
RMSE <sup>ls</sup>	0.15	0.10	0.27	0.93	3.98	12.1	5.5	0.33	0.33	0.020	
RMSE <sup>hc</sup>	0.68	0.46	0.50	0.74	2.84	78.5	83.6	0.69	1.32	0.010	Deepest largest magnitude.
RMSE <sup>lc</sup>	0.15	0.15	0.12	0.21	0.59	23.0	28.3	0.16	0.41	0.002	earthquake. Lake Mackay
RMSE <sup>hs</sup>	0.87	0.78	0.71	1.07	3.37	139.4	127.3	0.95	1.96	0.016	$M_w$ 6.7 (#1).
RMSE <sup>ls</sup>	0.26	0.24	0.15	0.32	0.97	41.7	37.3	0.22	0.54	0.003	
RMSE <sup>hc</sup>	0.34	0.20	0.86	18.23	3.44	33.5	18.9	0.23	1.03	0.041	Earthquakes $ U1  >  U2 $
RMSE <sup>lc</sup>	0.08	0.05	0.24	0.40	1.17	11.1	3.7	0.14	0.27	0.012	(transverse) excluding #8, #11, #19.
RMSE <sup>hs</sup>	0.62	0.39	1.39	19.66	7.81	71.6	27.4	0.30	1.41	0.075	
RMSE <sup>ls</sup>	0.15	0.11	0.32	0.61	2.46	22.6	6.7	0.17	0.36	0.024	
RMSE <sup>hc</sup>	0.23	0.24	0.44	7.84	5.03	32.2	18.5	0.19	0.34	0.025	Earthquakes $ U1  \leq  U2 $
RMSE <sup>lc</sup>	0.07	0.07	0.13	0.93	1.26	9.3	5.9	0.11	0.17	0.008	(normal) excluding #8, #11, #19.
RMSE <sup>hs</sup>	0.36	0.36	0.60	11.02	7.31	58.3	31.6	0.24	0.42	0.042	
RMSE <sup>ls</sup>	0.10	0.10	0.17	1.29	1.96	16.4	8.7	0.13	0.19	0.012	
RMSE <sup>hc</sup>	0.04	0.04	0.12	0.04	0.44	11.9	5.5	0.06	0.12	0.003	Earthquake Tennant Creek (#3).
RMSE <sup>lc</sup>	0.01	0.01	0.03	0.01	0.14	4.8	1.8	0.02	0.03	0.001	Well determined.
RMSE <sup>hs</sup>	0.09	0.07	0.38	0.05	1.43	35.8	10.2	0.09	0.27	0.010	
RMSE <sup>ls</sup>	0.02	0.02	0.05	0.02	0.25	10.7	3.5	0.03	0.04	0.002	

<sup>a</sup>Average Root Mean Square Error (RMSE) for selected simulations. Earthquake numbering is from Table 2. U1 is the left-lateral transverse component and U2 is the thrusting dip-slip component [e.g., Okada, 1985].

where  $n$  is the number of simulations,  $p_i^j$  the  $i$ th estimated parameter from the  $j$ th simulation, and  $\mu_i$  is the true value of the  $i$ th parameter. A summary of the computed simulations is provided in Table 3.

[31] We found that for magnitude  $\geq 5.8$  earthquakes the average RMSE of the horizontal components of the epicenter position was better than 0.07 km, depth 0.15 km, fault orientation was  $0.2^\circ$  and average slip was  $\sim 10$  mm, when observed in low noise conditions with ascending and descending observations, while with high noise observations the average RMSE of the epicenter was 0.3 km, depth was 0.5 km, fault orientation was  $2^\circ$  and average slip was  $\sim 30$  mm. In the simulations where only single geometry observations were considered (i.e., ascending or descending passes) the average RMSE of the epicenter, depth, fault orientation, and average slip was 0.3 km,  $2^\circ$  and 40 mm, respectively (averaged over low and high noise observations). This indicates that for moderate magnitude earthquakes, single geometry InSAR observations can still achieve good estimates of all source parameters (including fault orientation), although typically a combined geometry reduces the source parameter uncertainties by a factor of 1.5.

[32] For earthquakes of magnitude  $< 5.5$  the average RMSE of the epicenter was 0.3 km and depth was 0.5 km. We estimated the strike to better than  $1^\circ$ , and dip to better than  $3^\circ$ , for 67% of these earthquakes observed in the low noise scenario, while in the high noise scenario it was for 56% of these earthquakes. The high noise scenario resulted in some earthquakes not being visible by inspection of the interferogram (see Figure 5c).

[33] For the magnitude 5.0 (depth 1.3 km) Burakin earthquake we could estimate the epicenter of the rupture with an accuracy of  $\sim 0.1$  km, depth to 0.25 km and fault orientation to  $2^\circ$ . For the magnitude 4.8 (depth 1.5 km, dip  $79^\circ$ ) Burakin earthquake the solutions separated into two solution modes, the true fault plane (the RMSE of the strike  $< 2^\circ$ ) and its conjugate fault plane. However, in general, our results indicated that the observation of small magnitude (depth  $< 3$  km) earthquakes with InSAR will in the majority of cases provide useful estimates of earthquake source parameters.

[34] The most poorly estimated earthquake was the magnitude 6.2 Collier Bay (depth 10 km, dip  $84^\circ$ , rake  $153^\circ$ , #8 in Table 2) with the solutions failing to converge in both high and low noise scenarios. This earthquake had a



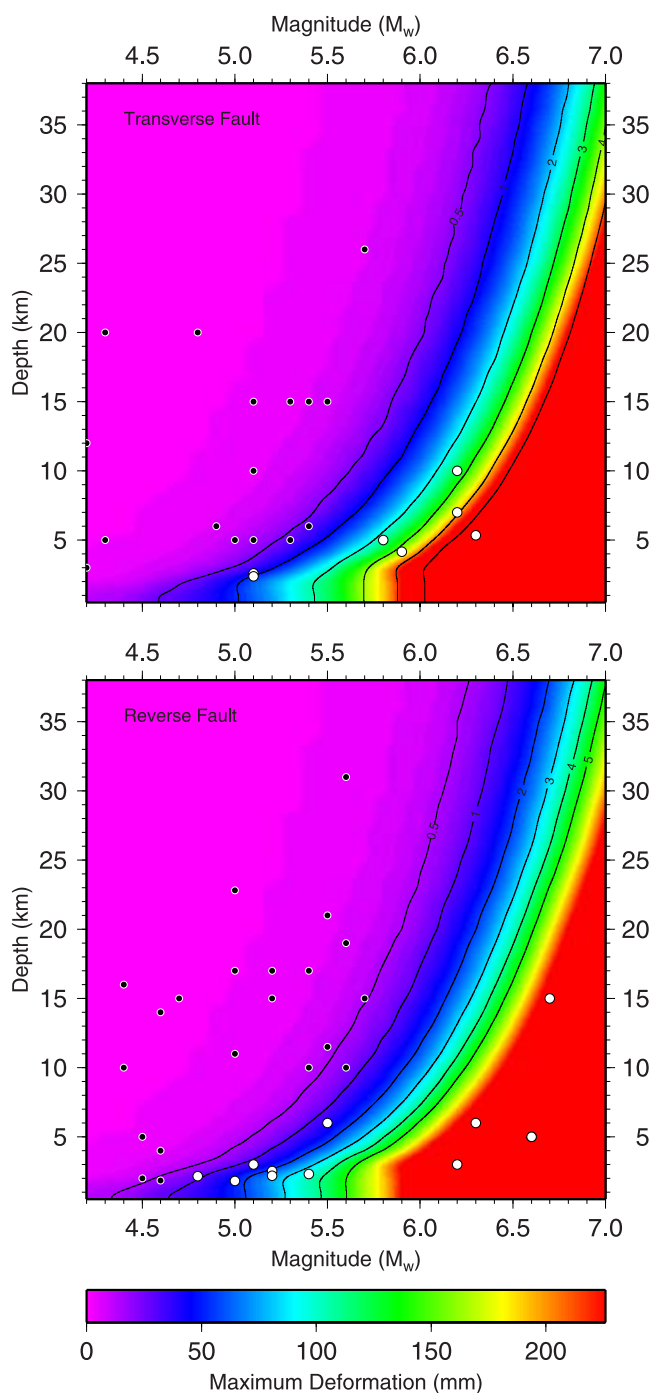


**Figure 6.** Simulated maximum InSAR visible deformation. (Top) Maximum deformation of pure transverse fault earthquakes. (Bottom) Maximum deformation of pure reverse fault earthquakes. View geometry is ENVISAT descending orbit. Fault patch dip is  $45^\circ$ , strike is  $180^\circ$ . Fault length, width and dislocation were computed from the adopted  $M_w$  and previously described methodology. The color scale is limited to a range of 0 to 226 mm (i.e., 0 to 8 28.3 mm fringes). The 0.5, 1, 2, 3, 4, 5 fringe (28.3 mm) deformation contours are shown. The plotted white circles are earthquakes from Table 2, while the black circles are the remaining earthquakes from Leonard *et al.* [2002] which do not generate visible surface deformation.

maximum simulated deformation of 76 and 88 mm for the descending and ascending pass interferograms respectively. The solution did however converge when we introduced an a priori constraint on the dip parameter. This indicates that InSAR is insensitive to magnitude 6.2 transverse earthquakes at 10 km depth; however, with the benefit of an a priori observation of the rupture dip, the other earthquake source parameters can be well estimated, at least to a comparable accuracy of equivalent magnitude earthquakes investigated in this study. The  $M_w$  5.5 Meckering (depth 6 km, #11 in Table 2) earthquake in the high noise scenario was also poorly determined. This earthquake had maximum deformation ranges of 34 mm for the descending and ascending pass interferograms. Thus a magnitude 5.5 earthquake that generates  $\sim 1$  fringe of deformation in the interferogram is resolvable by InSAR, but only in low observation noise conditions. These two earthquakes are at the threshold of the capability of InSAR to independently estimate earthquake parameters from surface deformation. This finding is consistent with previous studies of the observation of small magnitude earthquakes with InSAR, which include the magnitude 5.4 (depth 2.6 km) 1992 Landers aftershock [Feigl *et al.*, 1995], the magnitude 4.8 (depth  $\sim 2.2$  km), 5.3 (depth  $\sim 4.2$  km), 5.0 (depth  $\sim 3.5$  km), and 5.4 (depth  $\sim 5.3$  km) earthquakes in the Zagros Mountains, Iran, which required a priori constraints of the rupture strike Lohman2005, and the magnitude 5.6 (depth 9.4 km) Little Skull Mountain earthquake, which was jointly inverted with seismic data [Lohman *et al.*, 2002].

[35] To quantify the importance of the correct treatment of InSAR observational noise, we repeated the inversions of the 5 largest earthquakes, as well as the magnitude 5.8 Marryat Creek earthquake (#1 to #5 and #10 from Table 2) with uncorrelated, equally weighted observations. At the 95% confidence level we found no significant difference between the unweighted inversions and those more rigorously weighted by the 1-dimensional covariance functions, measured in terms of either the RMSE or the mean parameter bias. This is somewhat surprising given that in the high noise scenario observations are 50% correlated at 7.1 km and 25% correlated at 15.2 km, and indicates that the spatial sampling of InSAR observations is great enough to mitigate the effects of the high spatial correlation.

[36] For the earthquakes of magnitude  $< 5.4$  we observed a significant bias in the depth estimates, with an average bias of 0.2 km, systematically too shallow. For magnitude 4.8 (#19) the bias is 0.4 km, whereas for the magnitude 5.2 (#13) the bias is 0.09 km. This is significant given that the average depth of these earthquakes is 2.0 km. This bias is a direct consequence of the a priori constraints on the rupture dimension, which we applied for these small magnitude earthquakes. We found the rupture fault width is poorly separated from rupture depth for small magnitude earthquakes, and that the ratio of the error in width to the corresponding error in depth is 0.8.

[37] We divided the earthquakes into predominantly transverse (i.e.,  $|U1| > |U2|$ ) and normal/reverse type earthquakes (i.e.,  $|U1| \leq |U2|$ ). The average RMSE of the epicenters of the normal/reverse earthquakes are smaller than for transverse events ( $\sim 0.2$  km versus  $\sim 0.5$  km). While indicative only, this illustrates that InSAR is signif-

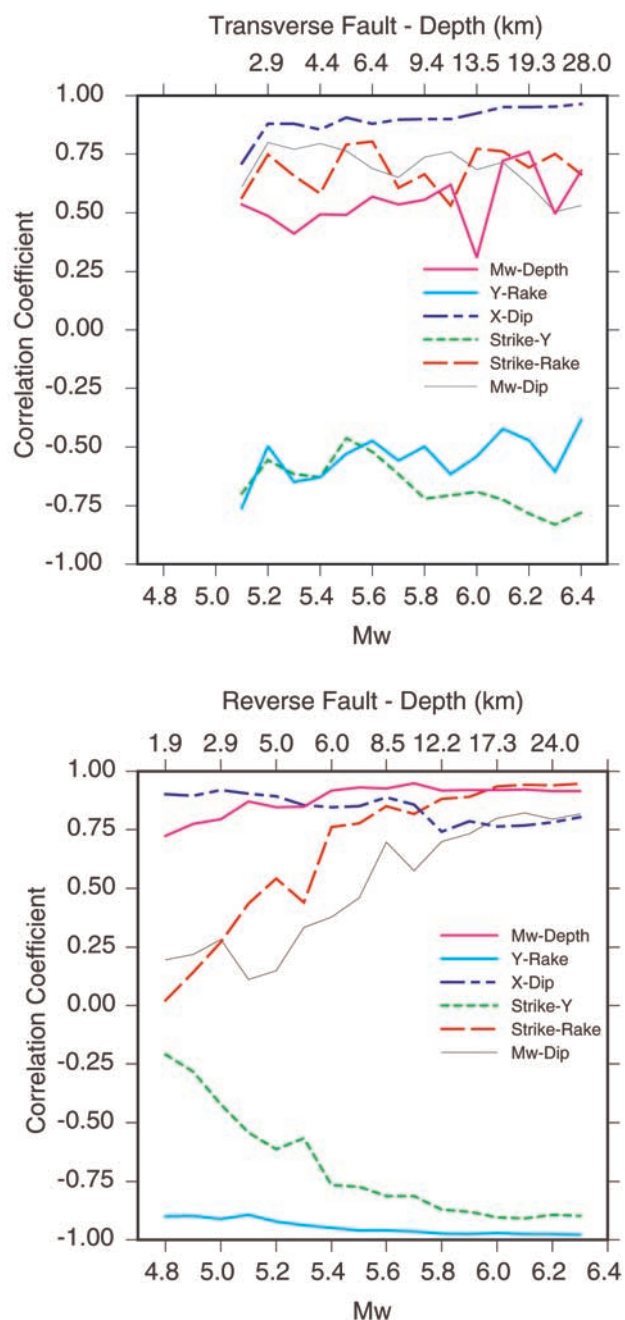


**Figure 7.** Parameter correlation coefficients computed from inversions along the 1-fringe deformation contour (i.e., Figure 6) plotted as a function of  $M_w$ .  $X$  and  $Y$  are the east and north coordinates of the earthquake respectively. The depth scale in non-linear. (Top) Transverse type fault. (Bottom) Reverse type fault.

icantly more sensitive to normal/reverse earthquakes by approximately half to one unit of magnitude. In Figure 6, we show the maximum deformation of pure reverse and transverse events, over which we plot each earthquake based on this classification.

[38] To further explore the InSAR sensitivities and parameter trade-offs we undertook further simulations of

pure reverse and transverse earthquakes along the 1-fringe deformation contour as shown in Figure 6. At magnitude intervals of 0.1 ( $M_w$ ) we generated 100 noise models to which we added the simulated earthquake deformation, which was no larger than 1-fringe (28.3 mm). That is as we increased the earthquake magnitude we also increased the depth so as to maintain consistent magnitude of surface deformation. For the reverse faults we simulated between magnitudes ( $M_w$ ) 4.8 and 6.3, while for the transverse earthquakes we simulated between magnitudes ( $M_w$ ) 5.1 and 6.4. We adopted a dip angle of  $45^\circ$  and strike of  $180^\circ$  and adopted the previously used low noise scenario.

[39] The source parameter estimation followed the previous procedures, except that for these inversions we adopted a point-source elastic dislocation model [Okada, 1985]. Specifically we inverted for magnitude, earthquake location and depth, and the strike, dip and rake of the rupture.

[40] In the majority of the inversions we were able to correctly differentiate between the actual fault plane and its conjugate fault plane. For the transverse fault case the correct fault plane was identified in 70% of cases while for the reverse fault case the correct fault plane was identified in 84% of cases. The percentage of correct fault plane identification remained constant as a function of magnitude/depth. We could further reduce the number of solutions converging to the conjugate fault plane by increasing the number of iterations of the inversion procedure (each with randomly selected prior values). Inversions which identified the conjugate fault plane were excluded from the subsequent correlation and trade-off analysis.

[41] In Figure 7 we show the computed correlation coefficients for the six most correlated parameter pairs. For the transverse faults the parameter correlations remain essentially unchanged as a function of earthquake magnitude/depth. However, for the reverse fault type earthquakes some the parameter correlations change as a function of magnitude. Specifically, the strike and  $y$ -coordinate (i.e., earthquake location in the north direction), the strike and rake, and the magnitude ( $M_w$ ) and dip parameters become more correlated as the magnitude/depth is increased. At magnitudes less than 5.5 and depth less than 6 km these parameters were well separable.

[42] In Figure 8 the estimated parameter bias (estimate minus truth) and the standard deviation of the parameter estimates are shown. For both earthquake types the precision of its location and depth decreases as the magnitude/depth of the earthquake increased. The precision of the rake, dip and strike are only weakly correlated to the earthquake magnitude and depth along the 1-fringe deformation contour. The rake estimates are more precise for the transverse type fault, however they are also more biased, presumably trading off against the earthquake location which is also somewhat biased. The depth estimates for the transverse type fault earthquakes are also systematically too deep and the earthquake magnitudes are too large.

## 5. Conclusions

[43] The precision of two-pass satellite SAR interferometry with ERS-2 and ENVISAT SAR data in the Australian

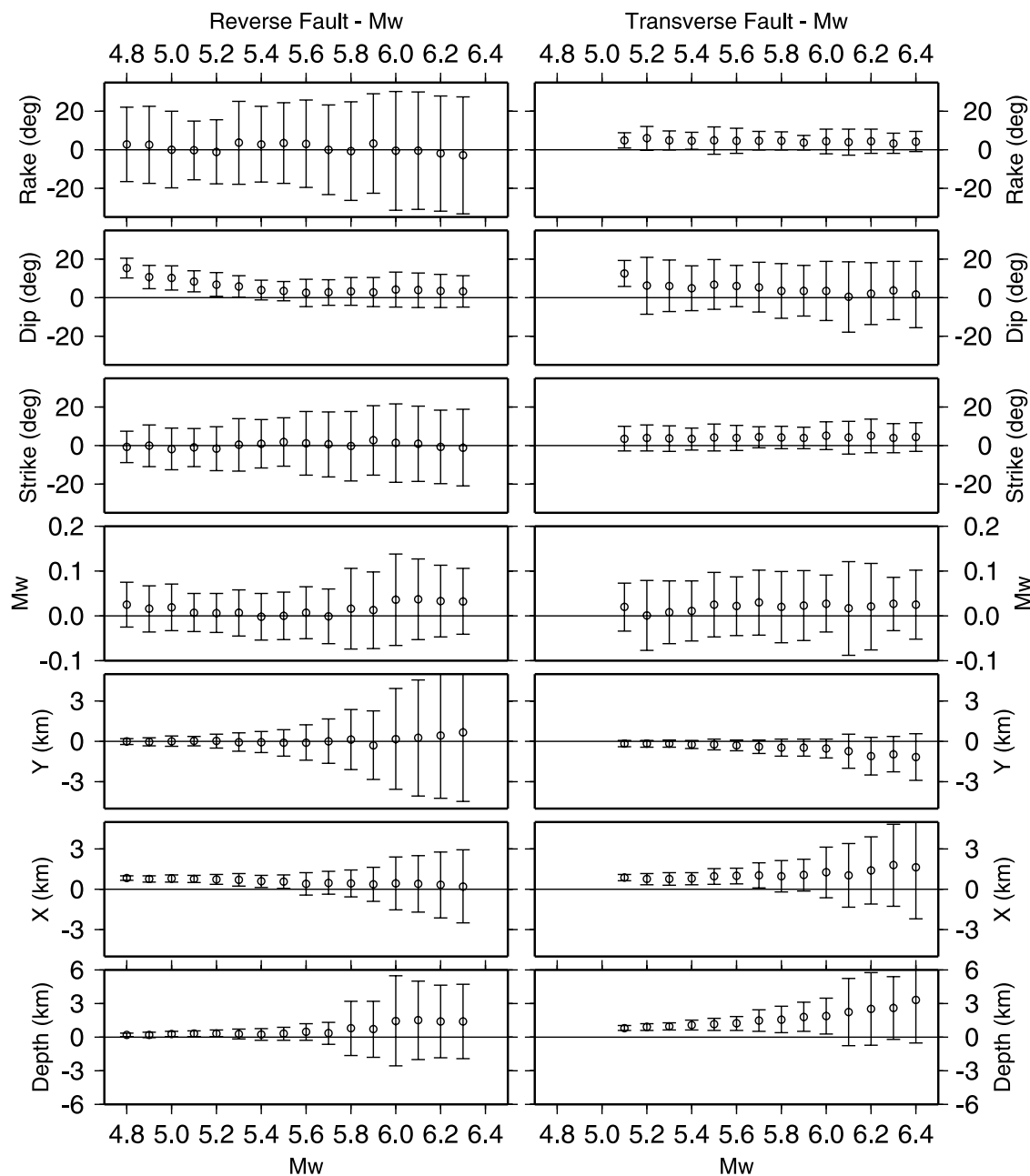


**Figure 8.** Parameter bias and precision computed from the inversions along the 1-fringe deformation contour (i.e., Figure 6) plotted as a function of  $M_w$ . The parameter bias is the average estimated value minus the truth, while the precision ( $1\sigma$ ) is represented by the error bars. (Left) Results from the reverse fault inversions. (Right) Results from the transverse fault inversions.

region can approach  $\pm 2$  mm ( $\sigma_{obs}$ ) and is routinely at the  $\pm 4$  mm level. Temporal variations of the order of 40 mm can occur due to spatial variation in atmospheric water vapor. Good quality interferograms were formed when perpendicular baseline lengths were less than 580 m and time between images of 175 days or less. We characterized the spectral noise of Australian InSAR interferograms and found that, while the absolute power of the noise power spectrum varies, the power law structure is consistent in all interferograms. On spatial scales of 0.5 to 2 km the spectral slope is dominated by atmospheric turbulence.

[44] In most cases single geometry (i.e., ascending or descending) InSAR observations can be used to accurately determine earthquake source parameters, although typically a combined geometry reduces the source parameter uncertainties by a factor of 1.5. We found no evidence that a failure to weight InSAR observations, as a function of inter-observation distance, in inversions for earthquake source parameters, produces biased parameter estimates or degrades the precision of inverted source parameters.

[45] We found for the majority of the earthquakes investigated that the fault plane and its conjugate fault plane were

well distinguished by InSAR observations, even with high noise observations.

[46] There is a significant reduction in the precision and accuracy estimates of InSAR inversions of surface deformation for magnitude 6.2 earthquakes deeper than 10 km and magnitude 5.5 events deeper than 6 km. However, InSAR can still be used to estimate epicenters, depths and focal mechanisms with accuracies comparable to solutions using teleseismic data. We have demonstrated that InSAR observations are capable of independently determining earthquake source parameters of earthquakes which deform the surface by as little as 28 mm, i.e., corresponding to a magnitude 4.8 earthquake at 1.6 km depth.

[47] In general, InSAR observations can be used to estimate typical intraplate earthquake source parameters with accuracies of  $\sim 0.3$  km for epicenter, depth to  $\sim 0.5$  km, fault dimensions to  $\sim 0.6$  km, strike and dip to a few degrees, slip to a few centimeters and magnitude to  $\sim 0.02$  ( $M_w$ ). Fault geometry can be estimated accurately even in cases where high observational noise prevents the visual identification of an earthquake in an interferogram. InSAR is significantly more sensitive to normal/reverse, than transverse type earthquakes by approximately one half to one full unit of earthquake magnitude.

[48] The trade-offs between the estimated source parameters vary as a function of magnitude/depth for a constant (absolute magnitude) expression of surface deformation. This magnitude/depth effect is particularly evident for reverse type faults.

[49] We identified 19 Australian earthquakes that have modeled displacements that would have been detectable from SAR observations, and a SAR-detectable earthquake occurs, on average about, every 2 years in Australia. Unfortunately, the data coverage in Australia is limited and the observation of any earthquakes in the period since the launch of the ERS-1 satellite in 1991 was not possible. Regions of high seismic risk should be imaged at a minimum temporal resolution of four scenes per year to enable InSAR to make a contribution to future co-seismic deformation investigations in Australia.

[50] **Acknowledgments.** The earthquake fault geometry inversions were computed on the Terrawulf Linux Cluster at the Centre for Advanced Data Inference, Research School of Earth Sciences, The Australian National University. STRM data is the void-filled seamless SRTM data V1, 2004, International Centre for Tropical Agriculture (CIAT), available from the CGIAR-CSI SRTM 90m Database: <http://srtm.csi.cgiar.org>. The non-conditional simulations were computed using the GSTAT software [Pebesma, 2004]. Figures were generated using the Generic Mapping Tools (GMT) software [Wessel and Smith, 1991]. ERS SAR data was processed by the Australian Centre for Remote Sensing (ACRES) and is copyright of the European Space Agency (ESA) 1995/1996/1997, all rights reserved. ENVISAT SAR data is copyright of ESA 2004/2005, Distribution Spot Image S.A., all rights reserved, and was purchased by Geoscience Australia. We thank Kurt Feigl and an anonymous reviewer for their helpful comments. The first author is currently on supported study leave from Geoscience Australia.

## References

- Agnew, D. K. (1992), The time-domain behaviour of power-law noises, *Geophys. Res. Lett.*, *19*, 333–336.
- Aki, K., and P. G. Richards (2002), *Quantitative Seismology, 2nd Ed.*, Univ. Science Books, Sausalito, California.
- Amelung, F., and J. W. Bell (2003), Interferometric synthetic aperture radar observations of the 1994 Double Spring Flat, Nevada, earthquake ( $M_{5.9}$ ): Main shock accompanied by triggered slip on a conjugate fault, *J. Geophys. Res.*, *108*(59), 2433, doi:10.1029/2002JB001953.
- Arnadottir, T., P. Segall, and M. Matthews (1992), Resolving the discrepancy between geodetic and seismic fault models for the 1989 Loma Prieta, California, earthquake, *Bull. Seismol. Soc. Am.*, *82*, 2248–2255.
- Atlantis-Scientific (2004), *EV-InSAR version 3.1 Users's Guide*, Atlantis Scientific Inc, Nepean, Ontario, Canada.
- Baran, I., M. Stewart, and S. Claessens (2005), A new functional model for determining minimum and maximum detectable deformation gradient resolved by satellite radar interferometry, *IEEE Trans. Geosci. Remote Sens.*, *43*, 675–682.
- Baumont, D., O. Scotti, F. Courboulex, and N. Melis (2004), Complex kinematic rupture of the Mw 5.9, 1999 Athens earthquake as revealed by the joint inversion of regional seismological and SAR data, *Geophys. J. Int.*, *158*, 1078–1087.
- Bos, A. G., S. Usai, and W. Spakman (2004), A joint analysis of GPS motions and InSAR to infer the coseismic surface deformation of the Izmit, Turkey earthquake, *Geophys. J. Int.*, *158*, 849–863.
- Burgmann, R., P. A. Rosen, and E. J. Fielding (2000), Synthetic aperture radar interferometry to measure earth's surface topography and its deformation, *Ann. Rev. Earth Planet. Sci.*, *28*, 169–209.
- Cressie, N. A. C. (1993), *Statistics for spatial data*, John-Wiley and Sons, INC., New York.
- Delouis, B., D. Giardini, P. Lundgren, and J. Salichon (2002), Joint inversion of InSAR, GPS, teleseismic, and strong-motion data for the spatial and temporal distribution of earthquake slip: Application to the 1999 Izmit mainshock, *Bull. Seismol. Soc. Am.*, *92*, 278–299.
- Feigl, K. L. (2002), Estimating earthquake source parameters from geodetic measurements, *International Handbook of Earthquake and Engineering Seismology*, *81A*, 607–620.
- Feigl, K. L., and E. Dupre (1999), RINGCHN: A program to calculate displacement components from dislocations in an elastic half-space with applications for modeling geodetic measurements of crustal deformation, *Comp. Geosci.*, *25*, 695–704.
- Feigl, K., A. Serpent, and D. Jacq (1995), Estimation of an earthquake focal mechanism from a satellite radar interferogram: Application to the December 4, 1992 Landers aftershock, *Geophys. Res. Lett.*, *22*, 1037–1040.
- Fialko, Y., M. Simons, and D. Agnew (2001), The complete (3-D) surface displacement field in the epicentral area of the 1999  $M_w$  7.1 Hector Mine earthquake, California, from space geodetic observations, *Geophys. Res. Lett.*, *28*, 3063–3066.
- Funning, G. J., B. Parsons, T. J. Wright, J. A. Jackson, and E. J. Fielding (2005), Surface displacements and source parameters of the 2003 Bam (Iran) earthquake from ENVISAT advanced synthetic aperture radar imagery, *J. Geophys. Res.*, *110*, B09406, doi:10.1029/2004JB003338.
- Gatelli, F., A. Guarnieri, F. Parizzi, P. Pasquali, C. Prati, and F. Rocca (1994), The wave-number shift in SAR interferometry, *IEEE Trans. Geosci. Remote Sens.*, *32*, 855–865.
- Ge, L., E. Cheng, D. Polonska, and C. Rizos (2002), Earthquake monitoring in Australia using satellite radar interferometry, *Wuhan Uni. J. Nat. Sci.*, *8*, 649–658.
- Ghiglia, D. C., and M. D. Pritt (1998), *Two-dimensional phase unwrapping: theory, algorithms, and software*, John Wiley, New York.
- Goldstein, R. (1995), Atmospheric limitations to repeat-track interferometry, *Geophys. Res. Lett.*, *22*, 2517–2520.
- Hanks, T. C., and H. Kanamori (1979), A moment-magnitude scale, *J. Geophys. Res.*, *84*, 2348–2350.
- Hanssen, R. F. (2001), *Radar interferometry, data interpretation and error analysis*, Kluwer Academic, Dordrecht, London.
- Jonsson, S. (2002), *Modeling volcano and earthquake deformation from satellite radar interferometric observations*, 174 pp., PhD Dissertation, Stanford Univ.
- Jonsson, S., H. Zebker, P. Segall, and F. Amelung (2002), Fault slip distribution of the 1999  $M_w$  7.1 Hector Mine, California, earthquake, estimated from satellite radar and GPS measurements, *Bull. Seismol. Soc. Am.*, *92*, 1377–1389.
- Just, D., and R. Bamler (1994), Phase statistics of interferograms with applications to synthetic aperture radar, *App. Opt.*, *33*, 4361–4368.
- Leonard, M., I. D. Ripper, and L. Yue (2002), Australian earthquake fault plane solutions, *Geoscience Australia, Record 2002/19*, p. 114.
- Lohman, R. B., and M. Simons (2005a), Locations of selected small earthquakes in the Zagros Mountains, *Geochem. Geophys. Geosyst.*, *6*, Q03001, doi:10.1029/2004GC000849.
- Lohman, R. B., and M. Simons (2005b), Some thoughts on the use of InSAR data to constrain models of surface deformation: Noise structure and data downsampling, *Geochem. Geophys. Geosyst.*, *6*, Q01007, doi:10.1029/2004GC000841.
- Lohman, R. B., M. Simons, and B. Savage (2002), Location and mechanism of the little skull mountain earthquake as constrained by satellite radar interferometry and seismic waveform modeling, *J. Geophys. Res.*, *107*(B6), 2118, doi:10.1029/2001JB000627.

- Massonnet, D., and K. L. Feigl (1995), Satellite radar interferometric map of the coseismic deformation field of the  $M = 6.1$  Eureka Valley, California earthquake of May 17, 1993, *Geophys. Res. Lett.*, *22*, 1541–1544.
- Massonnet, D., and K. L. Feigl (1998), Radar interferometry and its application to changes in the Earth's surface, *Rev. Geophys.*, *36*, 441–500.
- Massonnet, D., K. L. Feigl, H. Vadon, and M. Rossi (1996), Coseismic deformation field of the  $M = 6.7$  Northridge, California earthquake of January 17, 1994 recorded by two radar satellites using interferometry, *Geophys. Res. Lett.*, *23*, 969–972.
- McCue, K. (1990), Australia's large earthquakes and recent fault scarps, *J. Struct. Geol.*, *12*.
- Mellors, R. J., H. Magistrale, P. Earle, and A. Cogbill (2004), Comparison of four moderate-size earthquakes in southern California using seismology and InSAR, *Bull. Seismol. Soc. Am.*, *94*, 2004–2014.
- Michel, R., J. P. Avouac, and J. Taboury (1999), Measuring near field coseismic displacements from SAR images: Application to the Landers earthquake, *Geophys. Res. Lett.*, *26*, 3017–3020.
- Okada, Y. (1985), Surface deformation due to shear and tensile faults in a half-space, *Bull. Seismol. Soc. Am.*, *75*, 1135–1154.
- Pebesma, E. J. (2004), Multivariable geostatistics in S: The gstat package, *Comp. Geosci.*, *30*, 683–691.
- Pedersen, R., S. Jonsson, T. Arnadóttir, F. Sigmundsson, and K. L. Feigl (2003), Fault slip distribution of two June 2000  $M_w$  6.5 earthquakes in South Iceland estimated from joint inversion of InSAR and GPS measurements, *Earth Planet. Sci. Lett.*, *213*, 487–502.
- Press, W. H., S. A. Teukolsky, W. T. Vetterling, and B. P. Flannery (1992), *Numerical Recipes in C, The Art of Scientific Computing, Second Edition*, Cambridge Univ. Press, Cambridge.
- Pritchard, M. E., and M. Simons (2002), A satellite geodetic survey of large-scale deformation of volcanic centres in the central Andes, *Nature*, *418*, 167–171.
- Salichon, J., B. Delouis, P. Lundgren, D. Giardini, M. Costantini, and P. Rosen (2003), Joint inversion of broadband teleseismic and interferometric synthetic aperture radar (InSAR) data for the slip history of the  $M_w = 7.7$ , Nazca ridge (Peru) earthquake of 12 November 1996, *J. Geophys. Res.*, *108*(B2), 2085, doi:10.1029/2001JB000913.
- Sambridge, M. (1999a), Geophysical inversion with a neighbourhood algorithm - I. Searching a parameter space, *Geophys. J. Int.*, *138*, 479–494.
- Schmidt, D. A., and R. Burgmann (2006), InSAR constraints on the source parameters of the 2001 Bhuj earthquake, *Geophys. Res. Lett.*, *33*, L02315, doi:10.1029/2005GL025109.
- Scholz, C. H. (1990), *The mechanics of earthquakes and faulting*, Cambridge Univ. Press, Cambridge.
- Shamir, G., G. Baer, and A. Hofstetter (2003), Three-dimensional elastic earthquake modelling based on integrated seismological and InSAR data: the  $M_w = 7.2$  Nuweiba earthquake, gulf of Elat/Aqaba 1995 November, *Geophys. J. Int.*, *154*, 731–744.
- Simons, M., Y. Fialko, and L. Rivera (2002), Coseismic deformation from the 1999  $M_w$  7.1 Hector Mine, California, earthquake as inferred from InSAR and GPS observations, *Bull. Seismol. Soc. Am.*, *92*, 1390–1402.
- Talebian, M., J. Biggs, M. Bolourchi, A. Copley, A. Ghassemi, M. Ghorashi, J. Hollingsworth, J. Jackson, E. Nissen, B. Oveisi, B. Parsons, K. Priestley, and A. Saiidi (2006), The Dahuiyeh (Zarand) earthquake of 2005 February 22 in central Iran: reactivation of an intramountain reverse fault, *Geophys. J. Int.*, *164*, 137–148.
- Wells, D. L., and K. J. Coppersmith (1994), New empirical relationships among magnitude, rupture length, rupture width, rupture area, and surface displacement, *Bull. Seismol. Soc. Am.*, *84*, 974–1002.
- Wessel, P., and W. H. F. Smith (1991), Free software helps map and display data, *Eos Trans. AGU*, *72*, 441.
- Williams, S., Y. Bock, and P. Fang (1998), Integrated satellite interferometry: Tropospheric noise, GPS estimates and implications for interferometric synthetic aperture radar products, *J. Geophys. Res.*, *103*, 27,051–27,067.
- Wright, T. J. (2002), Remote monitoring of the earthquake cycle using satellite radar interferometry, *Phil. Trans. Royal Soc. London Series A-Math. Phys. Eng. Sci.*, *360*, 2873–2888.
- Wright, T. J., B. E. Parsons, J. A. Jackson, M. Haynes, E. J. Fielding, P. C. England, and P. J. Clarke (1999), Source parameters of the 1 October 1995 Dinar (Turkey) earthquake from SAR interferometry and seismic bodywave modelling, *Earth Planet. Sci. Lett.*, *172*, 23–37.
- Wright, T. J., B. E. Parsons, and Z. Lu (2004), Toward mapping surface deformation in three dimensions using InSAR, *Geophys. Res. Lett.*, *31*, L01607, doi:10.1029/2003GL018827.
- Zebker, H. A. (2000), Studying the earth with interferometric radar, *Comp. Sci. Eng.*, *2*, 52–60.
- Zebker, H. A., and J. Villasenor (1992), Decorrelation in interferometric radar echoes, *IEEE Trans. Geosc. Remote*, *30*.
- Zebker, H. A., P. A. Rosen, and S. Hensley (1997), Atmospheric effects in interferometric synthetic aperture radar surface deformation and topographic maps, *J. Geophys. Res.*, *102*, 7547–7563.

---

J. Dawson and P. Tregoning, Research School of Earth Sciences, The Australian National University, Building 61 Mills Road, Canberra, ACT 0200, Australia. (john.dawson@anu.edu.au)